A new method to compensate impedance artefacts for Li-ion batteries with integrated micro-reference electrodes

L.H.J. Raijmakers [a, b], M.J.G. Lammers [c], P.H.L. Notten [b, d], *

[a] Delft University of Technology, 2629 JB, Delft, The Netherlands
[b] Eindhoven University of Technology, 5600 MB, Eindhoven, The Netherlands
[c] NXP Semiconductors, 5656 AG, Eindhoven, The Netherlands
[d] Forschungszentrum Jülich (IEK-9), D-52425, Jülich, Germany

ABSTRACT

In order to measure the electrochemical characteristics of both electrodes inside Li-ion batteries, micro-reference electrodes (μREF) turned out to be very useful. However, measuring the electrochemical impedance with respect to μREF can lead to severe measurement artefacts, making a detailed analysis of the impedance spectra complicated. In the present work a new method is developed in which high-frequency measurement artefacts can be compensated. A theoretical analysis, using equivalent circuit models of the measurement setups, shows that if two different impedance measurements are averaged, the impedance contributions from the measurement leads can be completely eliminated. The theoretical analysis is validated using Li-ion batteries with seven integrated μREF, having all different impedances. The measurement results show that artefacts are dominating for high-impedance μREF in the high frequency range. However, these artefacts can be fully compensated by averaging two separate impedance measurements, as predicted by theory. This easily makes it possible to perform artefact-free impedance measurements, even at high frequencies.

© 2017 The Authors. Published by Elsevier Ltd. This is an open access article under the CC BY license (http://creativecommons.org/licenses/by/4.0/).

1. Introduction

Lithium-based batteries are today's most favourable systems to provide energy to battery powered applications, such as (Hybrid) Electric Vehicles ((H)EV), laptops and smartphones. Since (commercial) Li-ion batteries are two-electrode systems, only the total battery potential and impedance can be measured. However, for research purposes and to develop more advanced Battery Management Systems (BMS) it is of interest to distinguish between both electrodes with the use of reference electrodes (REF), hence making it possible to measure the electrochemical characteristics of the individual electrodes.

REF have already been introduced in many studies [1–14]. However, in particular Electrochemical Impedance Spectroscopy (EIS) measurements at three-electrode Li-ion battery systems are prone to measurement artefacts [15–26]. These artefacts cause a divergence in impedance spectra and, as a consequence, the

analyses of the measurements become unreliable and inaccurate. Moreover, underlying physical phenomena can be hidden by artefacts. Therefore, it is important to either prevent or to compensate these artefacts as much as possible.

Many studies on EIS measurement artefacts in the field of Li-ion batteries focuses on the cell geometry and/or the position of the REF, since improper three-electrode measurement setups are highly sensitive to artefacts. In general, it can be concluded that EIS measurement artefacts can be prevented to a large extend by using an appropriate cell geometry and REF position. Often these measurement setups are based on Swagelok-type cells in which perfect electrode alignment can be realized and where the REF can be easily introduced coaxially with respect to the electrodes [16,18,21,22]. Obviously, these setups are suitable for small-scale laboratory experiments. However, perfect electrode alignment and coaxially positioning of REF are more complicated to realize in large-size (commercial) Li-ion batteries, which are used in for example (H)EVs. Therefore these cells are often equipped with integrated micro-reference electrodes (μREF) [1,3,6,8,10,27].

Not only the cell geometry and electrode positions, but also the REF impedance and measurement equipment like, for instance cables, potentiostats, capillaries, frits, *etc.* can lead to EIS

measurement artefacts [15,24,28–34]. Obviously, the input impedance of the measurement device should be selected high and the REF impedance low [31]. Baker et al. [35] found by modelling and simulations that artefacts are a function of the REF size, its surface resistance, the resistance of the separator and both the working and counter electrodes. Furthermore, the length of the measurement cables should be reduced as much as possible [24,28], although this is sometimes difficult due to measurements which have to be performed at remote locations, such as gloveboxes and temperature-controlled climate chambers.

A solution to suppress high-frequency artefacts caused by the measurement equipment and the high-impedance REF, is to use so-called dual REF [29,32,33]. This is based on a second reference electrode which is carefully positioned in the cell and connected in series with a conventional REF through a capacitor. Recently, another successful technique is introduced in which a capacitor bridge between the counter electrode (CE) and the REF is used to suppress high-frequency EIS artefacts of three-electrode geometries [15]. The capacitor bridge balances the leakage current through the REF. However, it is not straightforward to determine the compensating value of the capacitor for systems, using dual REF or capacitor bridges. The capacitance must be carefully aligned to the measurement setup under consideration, which can lead to elaborate investigations.

This study presents a new method in which high frequency EIS measurement artefacts at three-electrode Li-ion batteries can be fully compensated by averaging two individual three-electrode EIS measurements. Strikingly, this results in artefact-free EIS measurements in the high frequency range of the impedance spectra, which is essential for e.g. characterizing the individual electrodes, for modelling purposes, State-of-Health indication and impedance-based temperature measurements [36–39]. The proposed method is similar to the method presented by Hsieh et al. [31], in which they correct artefacts arising from a so-called voltage divider effect. However, their work was performed on solid-state electrochemical devices in which the platinum REF impedance approaches the input impedance of the measurement device. Moreover, Hsieh et al. [31] combined one two-point and two three-point measurements in order to correct the artefacts, which is not required for the method presented in this work.

Models, including all electrode, device input and lead impedances are systematically developed in the present contribution in order to provide a deeper insight into the measurement artefacts of three-electrode Li-ion battery systems. It will be shown that the lead impedances, which can significantly contribute to artefacts, can be easily compensated by reversing the measurement device connections to the battery. In addition, multiple μREF with various active tip areas are used to investigate the influence of the REF impedance on the artefacts.

In order to experimentally show the artefacts and the strength of the proposed compensation method, EIS measurements are performed with conventional electrochemical measurement equipment on pouch-type Li-ion batteries with seven integrated μREF. The proposed compensation method is compared to the successfully applied capacitor bridging method, applied by Battistel et al. [15]. Finally, it will be shown that the impedance measurements can be accurately simulated by the developed artefact models.

2. Experimental

2.1. Battery construction

Pouch-type batteries are made with electrode dimensions of 72×190 mm (width x length). Each battery consists of six positive (P) and seven negative electrodes (N), which are separated by Celgard 2400 separators. Each electrode has an external current collector extension of 20×20 mm. A schematic representation of such an electrode stack is shown in Fig. 1a. The P and N electrodes are stacked in parallel and the complete battery stack is inserted into an Al-polymer pouch which is sealed after the electrolyte has been added. In order to put some pressure on the as-produced cells,
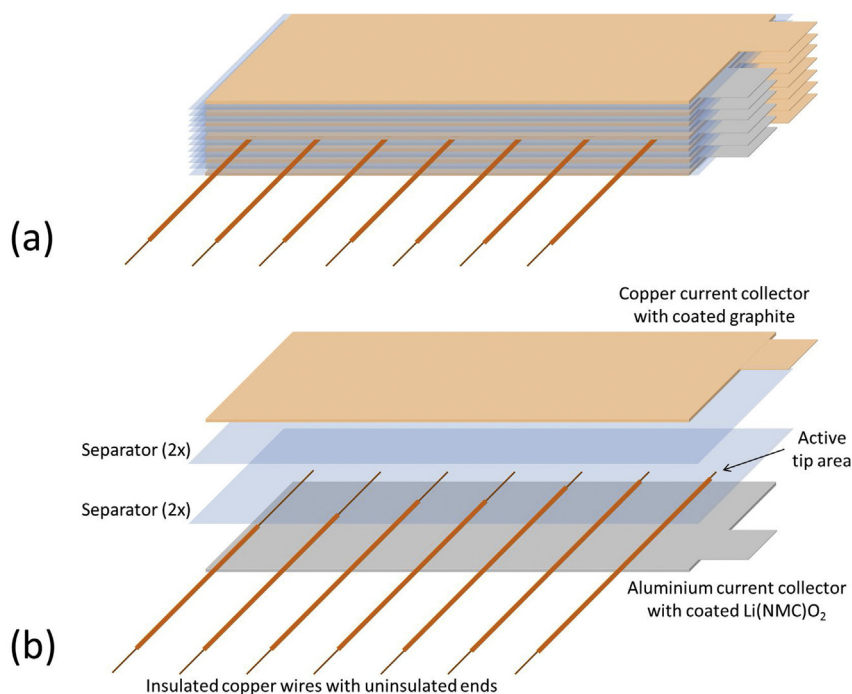
Fig. 1. Schematic representation of an electrode stack with seven integrated μREF (a) and enlargement of seven μREF in-between the P and N electrode (b). Note that on both sides of the μREF two separator sheets are used to isolate them from the electrodes.

the batteries are clamped between two solid plates connected with bolds.

The positive electrode material used in this study is Lithium Nickel Manganese Cobalt Oxide with composition $LiNi_{0.5}Mn_{0.3}Co_{0.2}O_2$ coated onto aluminium current collectors. Copper current collectors coated with graphite are used as negative electrodes. The pouch is filled with PuriEL battery electrolyte from Soulbrain (Korea) with composition of 1 M $LiPF_6$ in 1/1/1 ethylene carbonate/diethyl carbonate/ethyl methyl carbonate + 2 wt% vinylene carbonate solution.

2.2. Preparation of micro-reference electrodes

Insulated (Enamel) copper wires with radius of 100 μm and length of 300 mm are used as μREF. In total seven μREF are inserted into the battery with varying metallic Cu tip-lengths in order to investigate the influence of the μREF impedance on the measurement artefacts. The isolation at both ends is removed by immersing the wires into sulfuric acid, followed by rinsing in ethanol. The unprotected Cu wires, later acting as reference electrodes, are cut into seven different lengths, ranging from 0.5 to 50 mm in a logarithmic order. The other ends are used to make connection with the measurement equipment. Fig. 1b shows that the μREF are inserted transversely between four separator sheets (two on both sides) to prevent physical contact with the electrodes. Using this construction it can be assumed that the distance from the μREF to the positive and negative electrode is equal. The uninsulated ends are positioned in the central part of the battery stack.
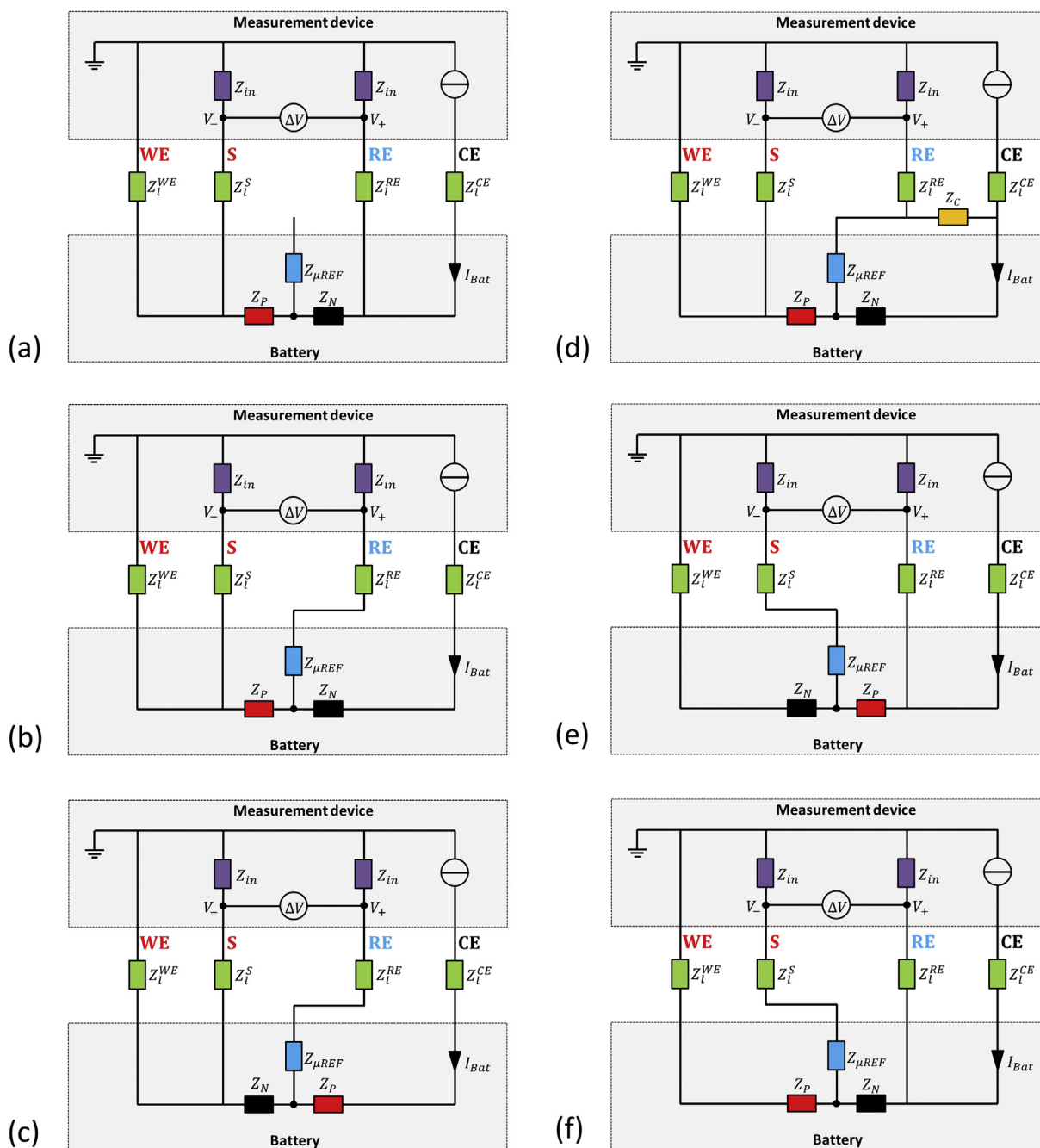
Fig. 2. Schematic equivalent circuits for EIS measurements at Bat (a), the P (b), the N (c), the P with capacitor bridge (d) the P with reversed connections (e) and the N with reversed connections (f).

2.3. Electrochemical measurements

Automatic battery cycling equipment (Maccor 2300) is used to activate and (dis)charge the batteries. Initially, all batteries are activated for four cycles using a constant current, constant voltage (CCCV) procedure. CC charging is performed with a current of 0.4 A until the cut-off voltage of 4.2 V is reached. Subsequently, the battery is charged at CV of 4.2 V till a cut-off current of 0.02 A has been reached. After charging a resting period of 2 h is applied followed by a 0.4 A discharge with a cut-off voltage of 2.7 V. In addition to these relatively low-current initialisation cycles, four cycles with a charge and discharge current of 2 and 4 A are applied. Finally, the nominal discharge capacity of 3.5 Ah is reached after full activation.

After activation the batteries are completely charged (CCCV) and metallic lithium is galvanostatically deposited onto the unprotected Cu tips of all μREF in order to get a stable lithium reference electrode potential. A 6 μm deposition layer thickness is chosen for all μREF. The lithium is deposited from both the P and N in order to obtain uniform layers around the wires. For a detailed description of the deposition and stability of lithium metal micro-reference electrodes, we refer to the work of Zhou and Notten [10].

Galvanostatic EIS measurements are performed at room temperature and at a voltage of 4.140 V for 50 logarithmically distributed frequencies in the range of 0.1 Hz–30 kHz with an Autolab PGSTAT302 N (Metrohm) and with an IviumStat (Ivium Technologies). The applied AC current excitation is set to 300 mA. This amplitude gave a good signal-to-noise ratio with optimum linear response. The EIS measurements are performed with complete batteries (Bat) and with the P and N electrodes measured with respect to all seven μREF.

The impedances of the individual μREF are also measured. However, since the impedances of the μREF are much larger than those of the batteries, the potentiostatic mode is now used. The applied voltage excitation is set to 1 mV for all μREF, except for the 0.5 mm μREF, which is set to 5 mV in order to increase the signal-to-noise ratio.

All measurements are performed in an argon-filled glovebox. The cable length of the measurement cables of the Autolab is 1.5 m and the cable length from the feedthrough to the battery inside the glovebox is approximately 2 m.

3. Theoretical considerations

EIS measurements on three-electrode Li-ion batteries can be prone to artefacts. Fig. 2 shows equivalent circuits which are used to derive models for simulating the impedances, including artefacts. Each equivalent circuit shows two (grey) rectangles, which represent the measurement device and the battery. The measurement device is highly simplified and consists of an ideal current source (θ), two input impedances (Z_{in}), a voltage measurement (ΔV) and a ground (≡). The connections to the measurement device are indicated with common abbreviations for electrochemical measurement equipment, *i.e.* WE for working electrode, CE for counter electrode, RE for the (μ)REF and S for the sense connection. The CE and WE serve as current-carrying cables and RE and S as voltage sense cables. This so-called four-point measurement configuration guarantees accurate measurements, although artefacts can still be present. The impedances of all measurement leads (Z_l^i) are shown between the measurement device and the battery. The battery is composed of impedances for P (Z_P), N (Z_N) and μREF ($Z_{\mu REF}$). For convenience all used symbols and abbreviations are listed in the nomenclature.

Using the equivalent circuits in Fig. 2, it is possible to derive mathematical models, which make it possible to simulate the

measured (^{m}) impedances of the total battery (Z_{Bat}^m), the positive (Z_P^m) and negative electrode (Z_N^m). It should be emphasized that these measured impedances can deviate from the true impedances for Z_{Bat}, Z_P and Z_N. This depends on the input impedances (Z_{in}) of the measurement device, the lead impedances (Z_l^i) and the μREF impedance ($Z_{\mu REF}$). In this section all measurement configurations shown in Fig. 2 will be discussed and modelled, including the configuration required to compensate for Z_l^i in the three-electrode measurement set-up.

3.1. Model assumptions

The equivalent circuits in Fig. 2 can easily be modelled by applying Kirchhoff's current and voltage laws. However, this approach makes it rather difficult to analytically investigate what elements are causing the measurement artefacts. Therefore, another approach is adopted in this study. For completeness and for the reader's interest the Kirchhoff law approach applied to the circuits in Fig. 2 can be found in Appendix A.

Fig. 2 shows that the battery excitation current (I_{Bat}) flows between the CE and WE connections of the measurement device and that the WE is connected to ground. The voltage response is measured between the RE and S connections, which are also connected to the ground through the input impedances Z_{in}. Since Z_{in} are input impedances it is assumed that their magnitudes are relatively large and equal. Therefore, it can be assumed that the currents through the S and RE leads are much smaller than I_{Bat}. For artefact-related modelling purposes it is, however, essential to also consider all lead and connection impedances. For simplicity reasons the lead and connection impedances of the WE (Z_l^{WE}), CE (Z_l^{CE}), RE (Z_l^{RE}) and S (Z_l^S) are considered equal.

3.2. Battery impedance

Adopting the simplified equivalent circuit in Fig. 2a, it is easy to derive a model for the measured battery impedance (Z_{Bat}^m). Therefore, it is first necessary to calculate the voltage response ΔV across P and N, which is measured between the RE and S of the measurement device

$$\Delta V = V_+ - V_-, \tag{1}$$

where V_+ is the voltage at the RE measured with respect to ground. It can be expressed as

$$V_+ = I_{Bat}\left(Z_N + Z_P + Z_l^{WE}\right)\frac{Z_{in}}{Z_{in} + Z_l^{RE}}, \tag{2}$$

where $I_{Bat}(Z_N + Z_P + Z_l^{WE})$ is the voltage across $(Z_N + Z_P + Z_l^{WE})$. However, since V_+ is measured between two impedances (Z_l^{RE} and Z_{in}) a so-called voltage divider is present and, therefore, the first term must be scaled with $Z_{in}/(Z_{in} + Z_l^{RE})$. Similarly, V_- determined at S with respect to ground can be calculated, according to

$$V_- = I_{Bat}Z_l^{WE}\frac{Z_{in}}{Z_{in} + Z_l^S}. \tag{3}$$

Subsequently, Z_{Bat}^m can be calculated by

$$Z_{Bat}^m = \frac{\Delta V}{I_{Bat}}. \tag{4}$$

Substituting Eqs. (1)–(3) into Eq. (4) leads to
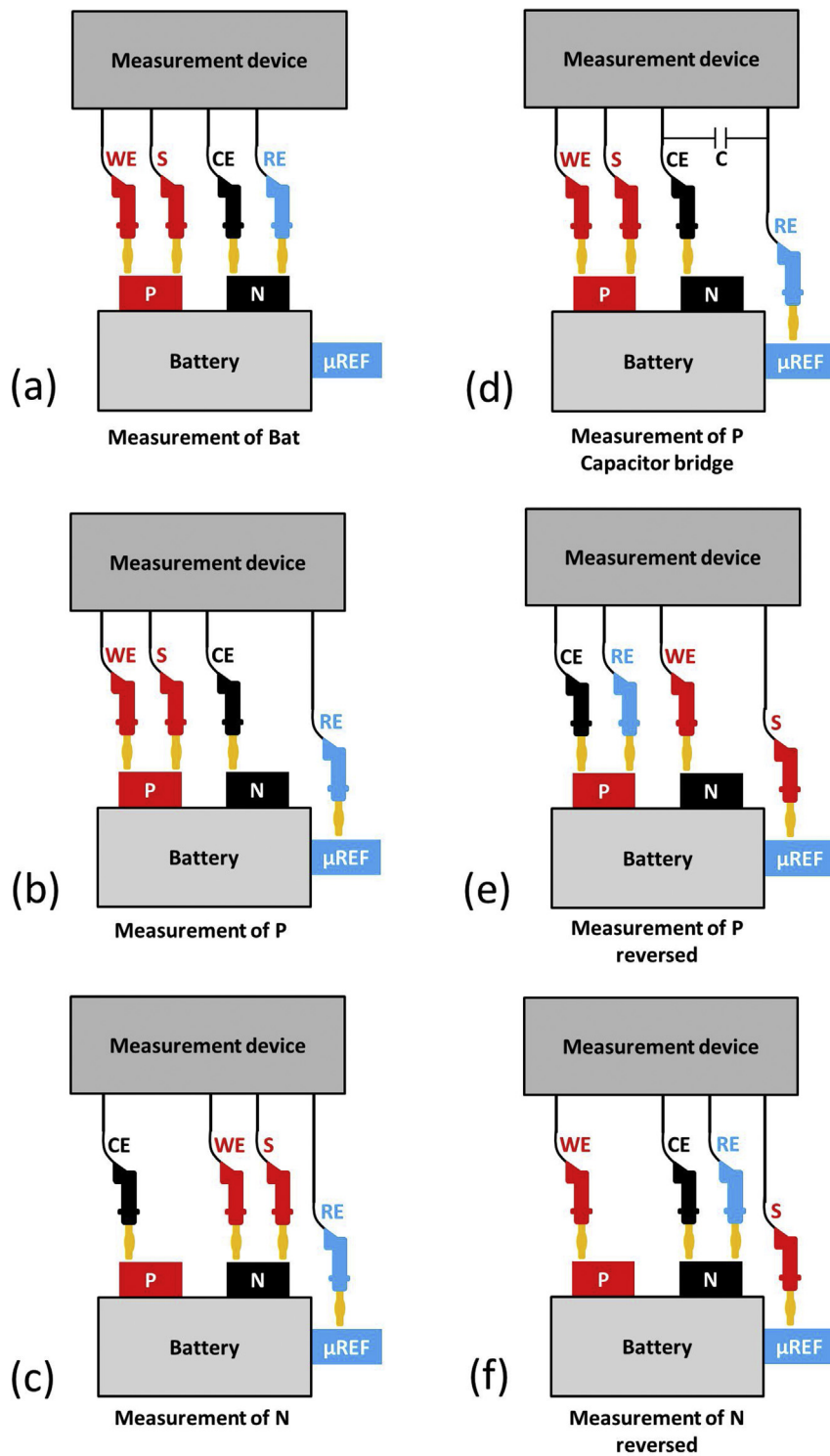
Fig. 3. Cable connections to measure EIS at a three-electrode battery. Connections to measure Bat (a), the P (b), the N (c), the P with capacitor bridge (d), the P with reversed connections (e), and the N with reversed connections (f).

$$Z_{Bat}^m = K_1(Z_N + Z_P) + Z_l^{WE}(K_1 - K_2), \tag{5}$$

where

$$K_1 = \frac{Z_{in}}{Z_{in} + Z_l^{RE}} \tag{6}$$

and

$$K_2 = \frac{Z_{in}}{Z_{in} + Z_l^S}. \tag{7}$$

K_1 and K_2 represent the as-denoted voltage dividers between the lead and input impedances. Obviously, Z_l^{RE} and Z_l^S in Eqs. (6) and (7) are much lower than Z_{in} and K_1 and K_2 therefore converge to 1. The total measured battery impedance in Eq. (5) can then be simplified to

$$Z_{Bat}^m = Z_N + Z_P. \tag{8}$$

From Eq. (8) it is obvious that the measured battery impedance is equal to the summation of the P and N impedances under normal measurement conditions. When the lead impedances Z_l^{RE} and Z_l^S are, however, not extremely small, K_1 and K_2 will not converge to 1 anymore, resulting in battery impedances, which will now include artefacts.

In Fig. 3a the connections how to measure the battery impedance are shown, which is experimentally the most conventional measurement configuration. WE and S are connected to the P of the battery whereas the CE and the RE are connected to the N of the battery.

3.3. Positive and negative electrode impedances

The equivalent circuit to measure the positive electrode impedance (Z_P^m) with respect to a reference electrode is shown in Fig. 2b. In this configuration the RE of the measurement device is connected to the μREF. The μREF impedance is now connected in series with Z_l^{RE}. This introduces an unbalance between RE and S (ΔV) because the μREF impedance is only present in the RE branch. Due to this unbalance, artefacts are likely to appear which can be understood in more detail by the following derivations.

The voltage response across P is measured between the RE and S. Considering $Z_{\mu REF}$, V_+ (Eq. (2)) has to be modified into

$$V_+ = I_{Bat}\left(Z_P + Z_l^{WE}\right)\frac{Z_{in}}{Z_{in} + Z_l^{RE} + Z_{\mu REF}}, \tag{9}$$

whereas the expression for V_- (Eq. (3)) remains the same. Following a similar derivation as for Z_{Bat}^m (Eq. (5)), Z_P^m can be represented by

$$Z_P^m = K_1 Z_P + Z_l^{WE}(K_1 - K_2), \tag{10}$$

where

$$K_1 = \frac{Z_{in}}{Z_{in} + Z_l^{RE} + Z_{\mu REF}} \tag{11}$$

and

$$K_2 = \frac{Z_{in}}{Z_{in} + Z_l^S}. \tag{12}$$

When Z_l^{RE} and Z_l^S are much lower than Z_{in}, K_2 can be considered unity again. However, K_1 in Eq. (11) now includes $Z_{\mu REF}$, which can be relatively large for small-sized μREF in Li-ion batteries as will be shown in Section 4.1 and may even approach Z_{in}. $Z_{\mu REF}$ can therefore not be neglected in this case. However, since K_2 still converges to 1, Eq. (10) can be simplified to

$$Z_P^m = K_1 Z_P + Z_l^{WE}(K_1 - 1). \tag{13}$$

From Eq. (13) it can be concluded that the lead impedance of the WE contributes to Z_P^m when K_1 in Eq. (11) does not converge to 1. In other words, the unbalance in the measurement setup caused by the μREF results in contributions from Z_l^{WE} multiplied with the negative gain ($K_1 - 1$). Voltage divider K1 is frequency dependent and always smaller than 1 (see Eq. (11)). Especially in the moderate and high frequency range, this will cause strong deviations in the impedance spectra. Particularly, the impedance spectra in the high frequency range, which are normally inductive, will bend towards the opposite, capacitive, direction. Obviously, this will lead to unfavourable artefacts in the impedance measurements of P, as will be shown and discussed in detail in Section 4. Furthermore, it can be seen that Z_N obviously does not occur in the expression for Z_P^m (Eq. (13)), indicating that its magnitude is not relevant in this configuration. The measured impedance for the negative electrode (Z_N^m) can be described in a similar way as for P, simply by replacing Z_N for Z_p in Eq. (13). The corresponding equivalent circuit is shown in Fig. 2c.

To experimentally determine the impedance of P with respect to μREF, RE of the measurement device must be connected to μREF, as indicated in Fig. 3b. The other cable connections can be the same as for measuring the total battery impedance in Fig. 3a. The cable connections to measure N are shown in Fig. 3c.

3.4. Capacitor bridge compensation

Battistel et al. [15] investigated the use of a capacitor bridge in order to compensate measurement artefacts in three-electrode geometries. Since Eq. (13) shows that artefacts can indeed be present, it seems to be a good solution to apply this bridge-method also in the case of three-electrode Li-ion batteries. An ideal capacitor bridge fully compensates the leakage current through μREF. That means that the net current through μREF should be zero for all measurement frequencies. Considering the equivalent circuit in Fig. 2d, the measured impedance of P in the presence of a capacitor bridge ($Z_{P,C}^m$) can be derived. It can be seen that a capacitor (Z_C) is positioned between μREF and N. In this approach we only assume that ideal capacitors are used. Hence, the current through the μREF is zero, making the voltage difference across Z_N equal to the voltage difference across Z_C. The current flowing through the capacitor (I_C) can then be given by

$$I_C = I_{Bat}\frac{Z_N}{Z_C}, \tag{14}$$

which leads to the following expression for V_+

$$V_+ = I_{Bat}\frac{Z_N Z_{in}}{Z_C}. \tag{15}$$

Since the current through the μREF is zero, V_+ can also be expressed as

$$V_+ = I_{Bat}\left(Z_P + Z_l^{WE}\right)\frac{Z_{in}}{Z_{in} + Z_l^{RE}}. \tag{16}$$

Eliminating V_+ from Eq. (16) by using Eq. (15) this leads after rearrangement to an expression for Z_C

$$Z_C = Z_N \frac{Z_{in} + Z_l^{RE}}{Z_P + Z_l^{WE}}. \tag{17}$$

Using Eq. (17) the value of the capacitor bridge can be calculated according to

$$C = \frac{1}{\omega |Z_C|}, \tag{18}$$

where ω is the angular frequency. Strikingly, from Eq. (17) it can be seen that the impedance of the capacitor bridge does not depend on the impedance of the µREF in the ideal situation. Furthermore, it can be seen that a large value for Z_{in} is more favourable as a lower capacitance can be used for compensation. Obviously, when the capacitor bridge is ideal, the measured impedance is equal to the true impedance of the electrodes, i.e. $Z_{P,\,C}^m = Z_P$ and $Z_{N,\,C}^m = Z_N$.

Fig. 3d shows the cable connections for measuring the impedance of P with respect to the µREF in the presence of a capacitor bridge. These cable connections are the same as without capacitor bridge (see Fig. 3b), except that a capacitor C is now positioned between RE and CE in Fig. 3d to compensate for the leakage current through µREF. In case of measuring N a capacitor should be positioned between RE and CE to fully compensate the artificial impedances.

3.5. Reversed electrode impedances

In order to compensate for high-frequency artefacts arising from the measurement leads, a new measurement concept is proposed in which the cable connections from the measurement device to the battery are simply reversed with respect to a standard configuration. The schematic equivalent circuit for this reversed connection concept is shown in Fig. 2e. It can be seen that this measurement setup reveals the same unbalance with respect to Fig. 2b, but now it is reversed. Z_P^m for the reversed configuration ($Z_{P,\,r}^m$) can be derived similarly as for the standard configuration. The resulting expression for $Z_{P,\,r}^m$ in the reversed configuration then becomes

$$Z_{P,\,r}^m = K_2 Z_P + \left(Z_N + Z_l^{WE} \right)(K_2 - K_1), \tag{19}$$

where

$$K_1 = \frac{Z_{in}}{Z_{in} + Z_l^S + Z_{\mu REF}} \tag{20}$$

and

$$K_2 = \frac{Z_{in}}{Z_{in} + Z_l^{RE}}. \tag{21}$$

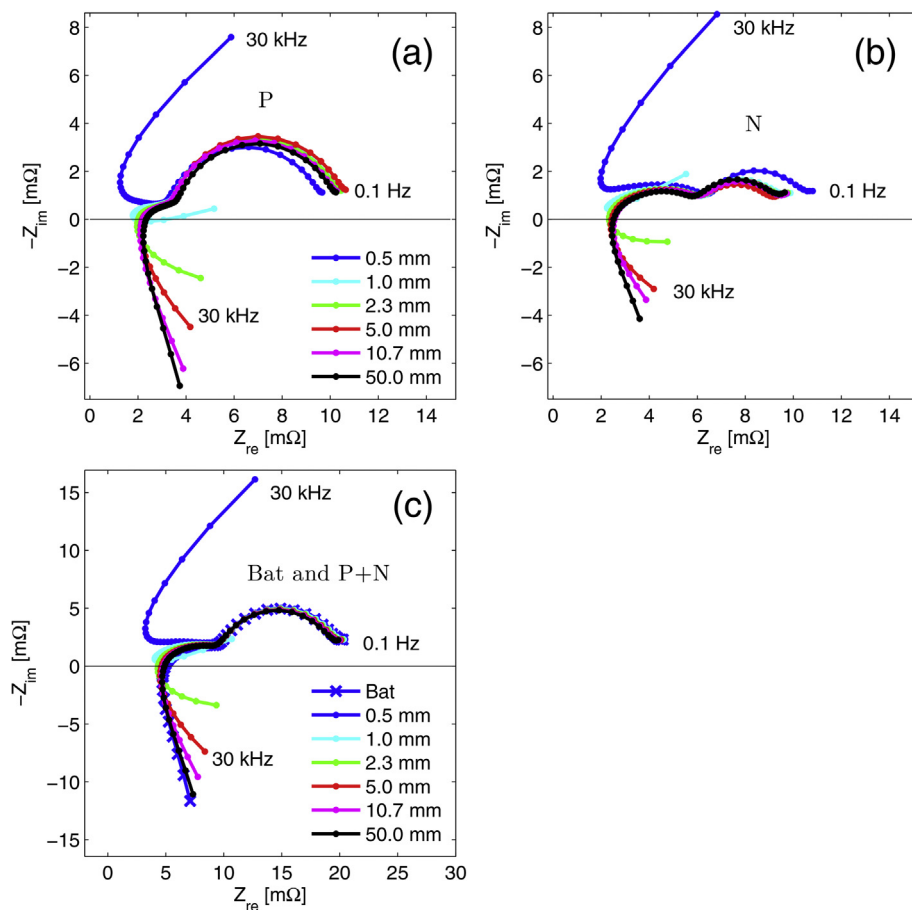As $Z_l^{RE} = Z_l^S < < Z_{in}$ it can be seen from Eq. (21) that K_2 approaches 1.

Fig. 4. Impedances of P (a) and N electrode (b) measured with respect to µREF with different tip-lengths. Comparison of the measured battery impedance (Bat) and the summation of P and N (c). For clarity reasons the results for the 23.2 mm long µREF are excluded.

Eq. (19) can then be reduced to

$$Z_{P,r}^m = Z_P + \left(Z_N + Z_l^{WE}\right)(1 - K_1). \tag{22}$$

From Eq. (22) it can be concluded that both Z_N and Z_l^{WE} contribute to $Z_{P,\ r}^m$ if K_1 does not converge to 1. This will again result in measurement artefacts. Voltage divider K1 is frequency dependent and always smaller than 1. $(Z_N + Z_l^{WE})$ is multiplied with a small positive gain $(1 - K_1)$ and this product contributes to $Z_{P,\ r}^m$, especially at high frequencies. Particularly, the inductive tail will be extended in the same direction. The effect explained in Section 3.3, in which impedance spectra deviate to the opposite direction can therefore be compensated by using the reversed configuration. The measured impedance for the reversed N ($Z_{N,\ r}^m$) can be calculated similarly as for the reversed P ($Z_{P,\ r}^m$) by replacing Z_p by Z_N and Z_N by Z_p in Eq. (22). The corresponding electronic network scheme is shown in Fig. 2f.

In Fig. 3e shows the cable connections to experimentally determine the impedance of P *vs* µREF in the reversed cable connection set-up. In this configuration WE changes position with CE and S with RE in comparison to the standard configuration (Fig. 3b). The connections to measure the reversed N impedance spectra are shown in Fig. 3f.

3.6. Lead impedance compensation

The contribution of Z_l^{WE} (Eqs. (13) and (22)) can now easily be compensated by averaging the standard and reversed configurations. Therefore, the measurement artefacts contributing from the lead impedances can be fully compensated. Obviously, this does not work if the impedance of N is much larger than that of P (see Eq. (22)). However, in (commercial) Li-ion batteries the impedance of both electrodes are of the same order of magnitude. Taking the average of Eqs. (13) and (22) leads to

$$\overline{Z_P^m} = \frac{1}{2}\left\{Z_P^m + Z_{P,r}^m\right\} = \frac{1}{2}\{Z_P(1 + K_1) + Z_N(1 - K_1)\}, \tag{23}$$

where

$$K_1 = \frac{Z_{in}}{Z_{in} + Z_l^S + Z_{\mu REF}} \tag{24}$$

in which $Z_l^S = Z_l^{RE}$. If $Z_l^{RE} = Z_l^S << Z_{in}$, K_1 can be reduced to

$$K_1 = \frac{Z_{in}}{Z_{in} + Z_{\mu REF}}. \tag{25}$$

From Eq. (23) it can be concluded that Z_l^{WE} has been cancelled out despite the fact that it is always present in the expressions for the standard and reversed configurations (Eqs. (13) and (22)). This implies that this simple averaging method gives us the opportunity to fully compensate for the lead impedances, which can be a significant source of measurement artefacts, especially for measurements at remote locations using long measurement leads. The compensated impedance for N ($\overline{Z_N^m}$) can be calculated in a similar way as for P ($\overline{Z_P^m}$), by replacing Z_p by Z_N and Z_N by Z_p in Eq. (23).

Note that reversing the cable connections (Fig. 3e and f) essentially only needs to be done with WE and CE to let this method work. Reversing S and RE is only done in order to get the impedance spectra in the correct complex plane quadrant during the measurements. Obviously, this can also be performed by post-processing the measurement data.

The proposed averaging impedance concept results in five individual impedance measurements, *i.e.* the battery impedance and

the impedances of the P and N electrodes in both the standard and reversed configuration. The impedance measurement at the battery (Fig. 3a) only has to be performed once since reversing the cable connections has obviously no influence on the battery result, which can be easily mathematically validated by considering the derivations described in Section 3.2 for the reversed configuration. The explained measurement concept will be experimentally investigated using multi-electrode batteries. These results are described in the following Section.

4. Results and discussion

4.1. Positive and negative electrode impedances

Fig. 4a and b shows the measured impedances for the P and N electrodes, respectively, measured with respect to six different µREF. Measurement artefacts can clearly be seen, especially in the high frequency range of the spectra. The artefacts are most dominant for the µREF with the smallest active tip-length of 0.5 mm and they strongly reduce with increasing tip length. It can be seen that the P and N impedance spectra are curling upwards in the high frequency range. It is obvious that these impedance measurements are highly influenced by the measurement setup configuration. On the other hand, the mid-frequency and low frequency range are showing the expected characteristic semicircles.

Fig. 4c shows the impedance summations (P + N) of the P and N spectra measured according to Figs. 2b and 3b together with the measured impedance for the complete battery (Figs. 2a and 3a). In the high frequency range the added spectra clearly show large discrepancies with respect to that of the battery (Bat). This
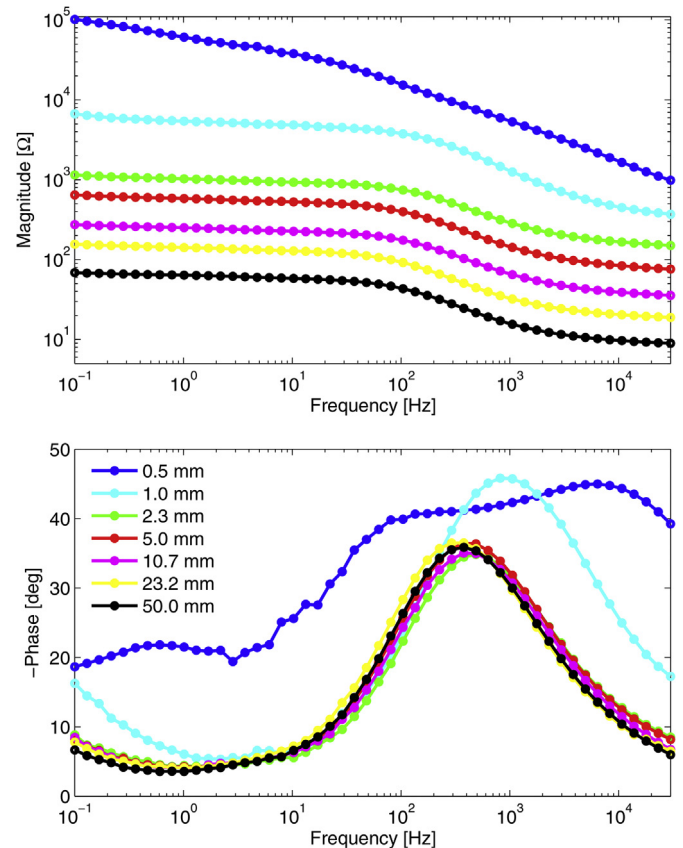

Fig. 5. Bode plots of the various µREF measured with respect to the low-impedance P electrode. The tip length of the µREF are indicated in the legend.

especially holds for the µREF with short tip lengths and strongly reduces for increasing lengths. The µREF with a tip length of 50 mm shows the best results in comparison to Bat and is, therefore, favourable to use in this battery configuration. For the low frequency range it can be concluded that the summation of the P and N are in perfect agreement with the Bat results.

Evidently, these measurement results reveal that the high frequency part suffers from measurement artefacts, especially for µREF with short tip lengths. In order to investigate the µREF characteristics in more detail, their impedances are measured with respect to the low-impedance P electrode. The results are shown in the Bode plots of Fig. 5. From these measurements it can be seen that the µREF with an active tip length of 0.5 mm (blue line) has the highest impedance and that with an active tip length of 50 mm (black line) reveals the lowest impedance. Decreasing impedances with increasing tip lengths are indeed to be expected as the active surface area of the 50 mm tip is about two orders of magnitude larger than that of the 0.5 mm tip.

Following the mathematical analysis in Section 3, in particular K_1 (see for example Eqs. (11) and (20)), it is evident that the measured artefacts become more dominant for µREF with smaller tip lengths. The reason is that K_1 will not converge to 1 anymore when the µREF impedance becomes too large. For the µREF with the smallest tip length (0.5 mm) this effect is the most dominant and

the measured electrode impedance starts to deviate. Since the gain $(K_1 - 1)$ in Eq. (13) is negative the high frequency inductive impedance spectra in Fig. 4 bend towards the capacitive region. With increasing tip lengths, K_1 starts to converge to 1 and the gain $(K_1 - 1)$ therefore decreases. This results in a reduction of the artefacts, which now appear clockwise towards the inductive region.

As almost artefact-free impedance spectra can be measured with large surface area µREF (see Fig. 4), the 0.5 mm µREF is used in the following sections in order to show that the presented compensation method properly operates. Obviously, the compensation method is effective for all µREF, independent on its surface area.

4.2. Capacitor bridge compensation

Fig. 6a shows the uncompensated EIS measurement results for Bat (dark blue curve) and for P (light blue curve) and N (green curve) measured with respect to the µREF with a tip length of 0.5 mm. As concluded in Section 4.1 the P and N measurements severely suffer from artefacts in the high frequency range. Obviously the summation curve (red curve in Fig. 6a) also clearly reveals the presence of these artefacts in the high frequency range. However, the summation curve agrees perfectly well with the measured Bat curve in the low frequency range.
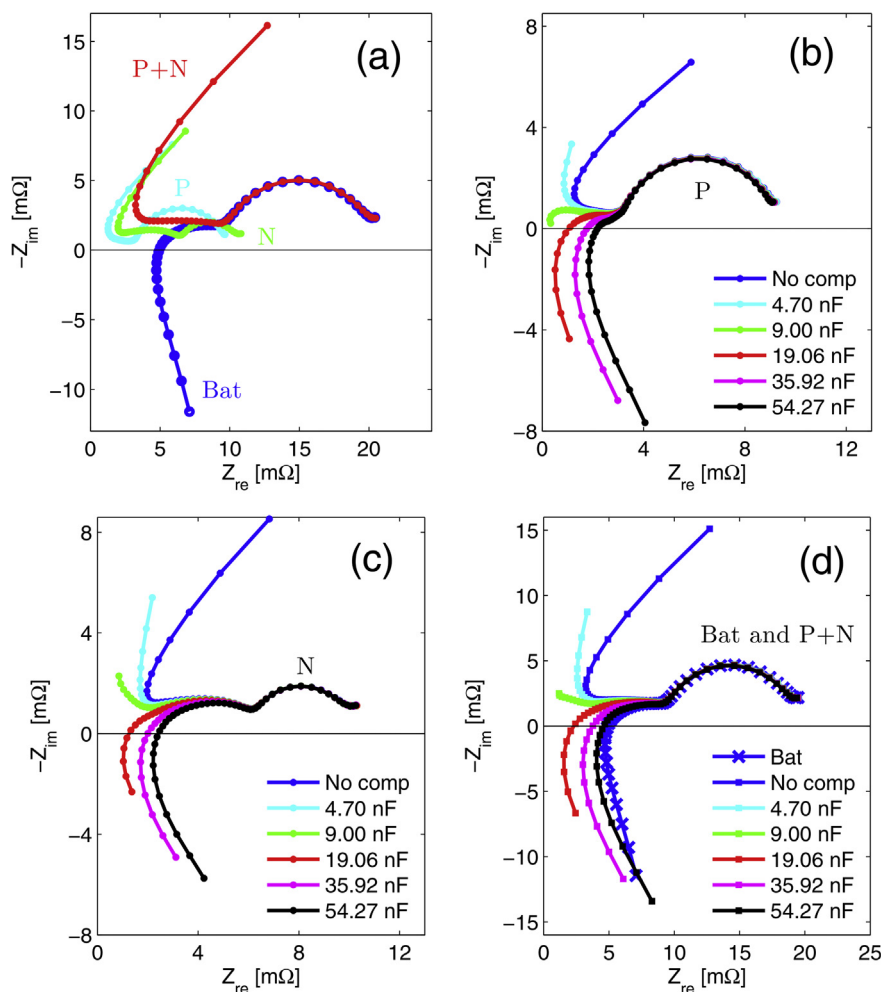
Fig. 6. EIS measurements at Bat and both the individual P and N electrode measured with respect to the µREF with active tip length of 0.5 mm and summation (P + N) impedance curve (a). EIS measurements without capacitor compensation (No comp) and with capacitor compensation at the P (b) and N electrode (c). Comparison of Bat impedance spectrum and all summation curves of P + N (d).
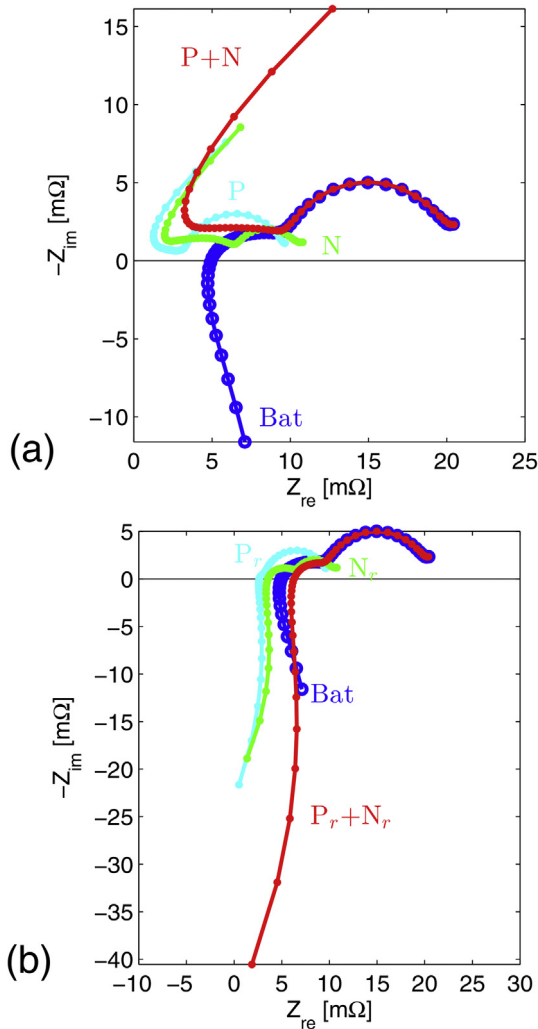
Fig. 7. Measurement artefacts in the high frequency range of the impedance spectra measured with a standard cable connection configuration (a) and with reversed cable connection set-up (b).
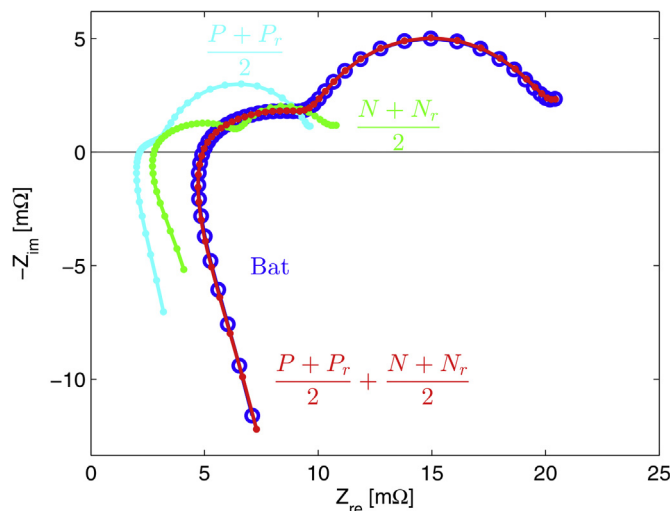
Fig. 8. Artefacts compensated impedance spectra. EIS measurements for the P and N are performed on a μREF with an active tip length of 0.5 mm.

Fig. 6b shows the various compensated EIS measurements of the P electrode with respect to the μREF with tip length of 0.5 mm. For these measurements various off-the-shelf capacitors have been placed between RE and CE in accordance with Figs. 2d and 3d to compensate for leakage currents. The EIS measurement without using a capacitor bridge is also shown as reference (dark blue curve). From these results it can be concluded that the high-frequency artefacts systematically decrease with increasing capacitor values. The same measurements have been performed for N with respect to the μREF with a tip length of 0.5 mm and similar results are found as shown in Fig. 6c.

In order to verify which capacitor value would be the most optimal compensation for the present artefacts, the P and the N impedance are added together for each capacitor and compared to the impedance spectrum of Bat (Fig. 6d). These results show that the capacitors with values 35.92 nF (pink curve) and 54.27 nF (black curve) are in close agreement with the Bat result (dark blue curve). These values are comparable to the 100 nF capacitor, which was also favourably selected by Battistel et al. [15]. Using higher capacitor values would lead to higher discrepancies between Bat and the summation of P and N.

From these results it can be concluded that tuning a capacitor bridge to the battery system under consideration is not straightforward and is quite time-consuming. Moreover, relative large deviations in the high frequencies can still be found between the summation of P and N in comparison to Bat (Fig. 6d). Consequently, an accurate EIS analyses of the high frequency part of the individual electrodes is unfortunately not possible.
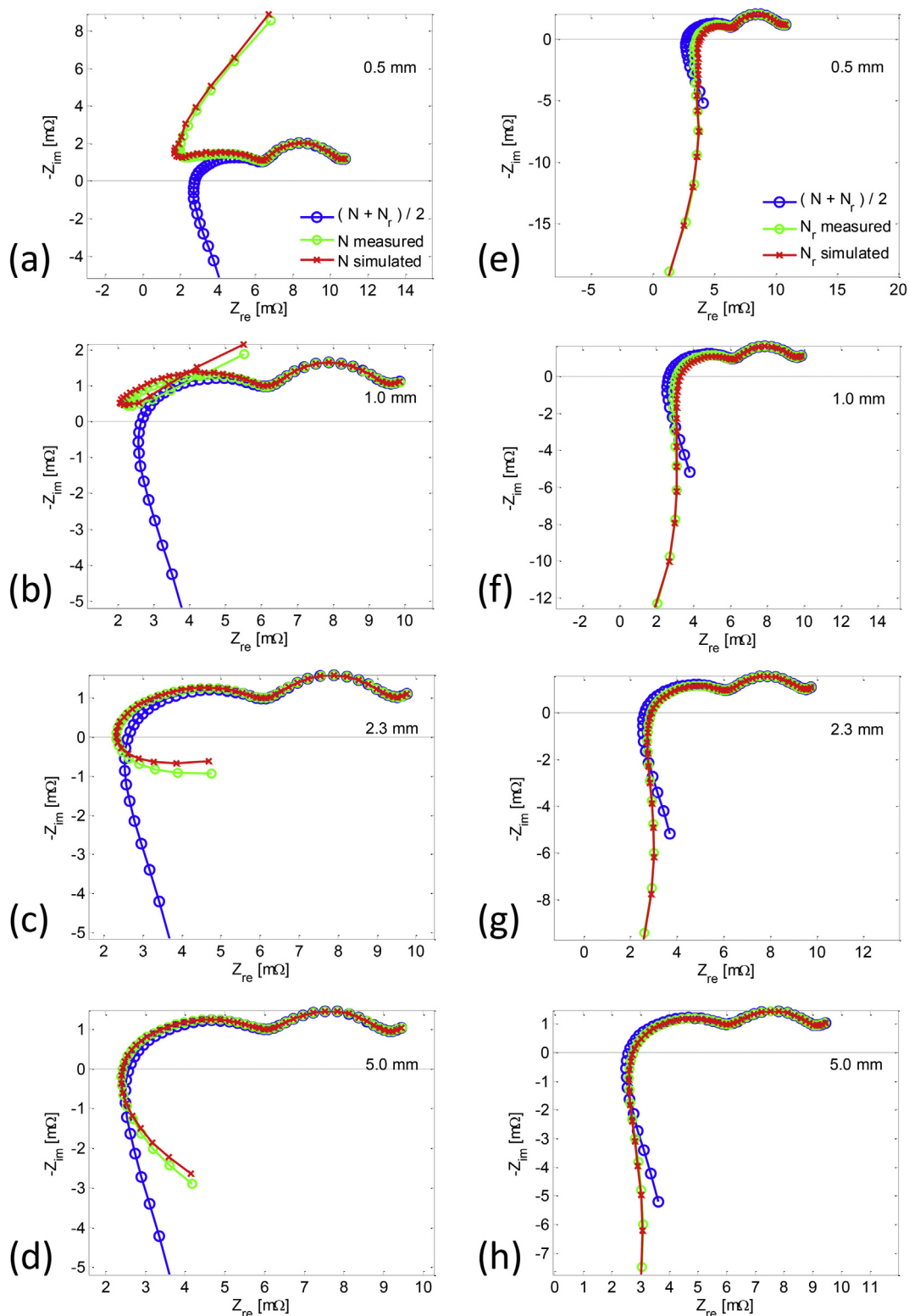
4.3. Lead impedance compensation

In Section 3 a new concept has been proposed to compensate for the high-frequency EIS measurement artefacts, simply by reversing the measurement cables. In Fig. 7 the measured impedance spectra for all measurement combinations described in Section 3 are shown in the complex plane. Both P (light blue curve) and N (green curve) impedances are measured with respect to μREF with an active tip length of 0.5 mm. Also the summations of the P and N impedance spectra (red curve) for both the standard and reversed measurements are shown. The Bat results are represented by the dark blue curve.

Fig. 7a shows the measured impedance spectra with the cables in the standard measurement configuration in accordance to the connections shown in Fig. 3a, b and c. The same measurement results are also shown in Fig. 6a, but are reproduced here in order to properly compare with the results obtained with the reversed cable connections in Fig. 7b.

Fig. 7b shows the impedance results obtained with the cables in the reversed connections, i.e. according to the connections shown in Fig. 2a, e and f. For the reversed impedance measurements of the positive and negative electrode (P_r and N_r) it can be seen that a high frequency tail is located in the inductive region (positive imaginary values) of the impedance. However, the tails are reaching relatively far in the inductive area and also bend somewhat to the left, which is atypical for inductive behaviour. From the reversed measurements it can clearly be seen that the artefacts are moving into the opposite direction in comparison to the standard configuration of Fig. 7a. These experiments prove the theory, which has been described in Section 3.5. The gain $(1 - K_1)$ is positive due to the unbalance in this measurement configuration and, therefore, the inductive tail is extended into the inductive region (see Eq. (22)). Furthermore, Fig. 7b shows that the $P_r + N_r$ curve does not match Bat either in the high frequency range. Like for the standard measurement configuration (Fig. 7a), the summation curves are only in good agreement with the Bat result in the low frequency range.
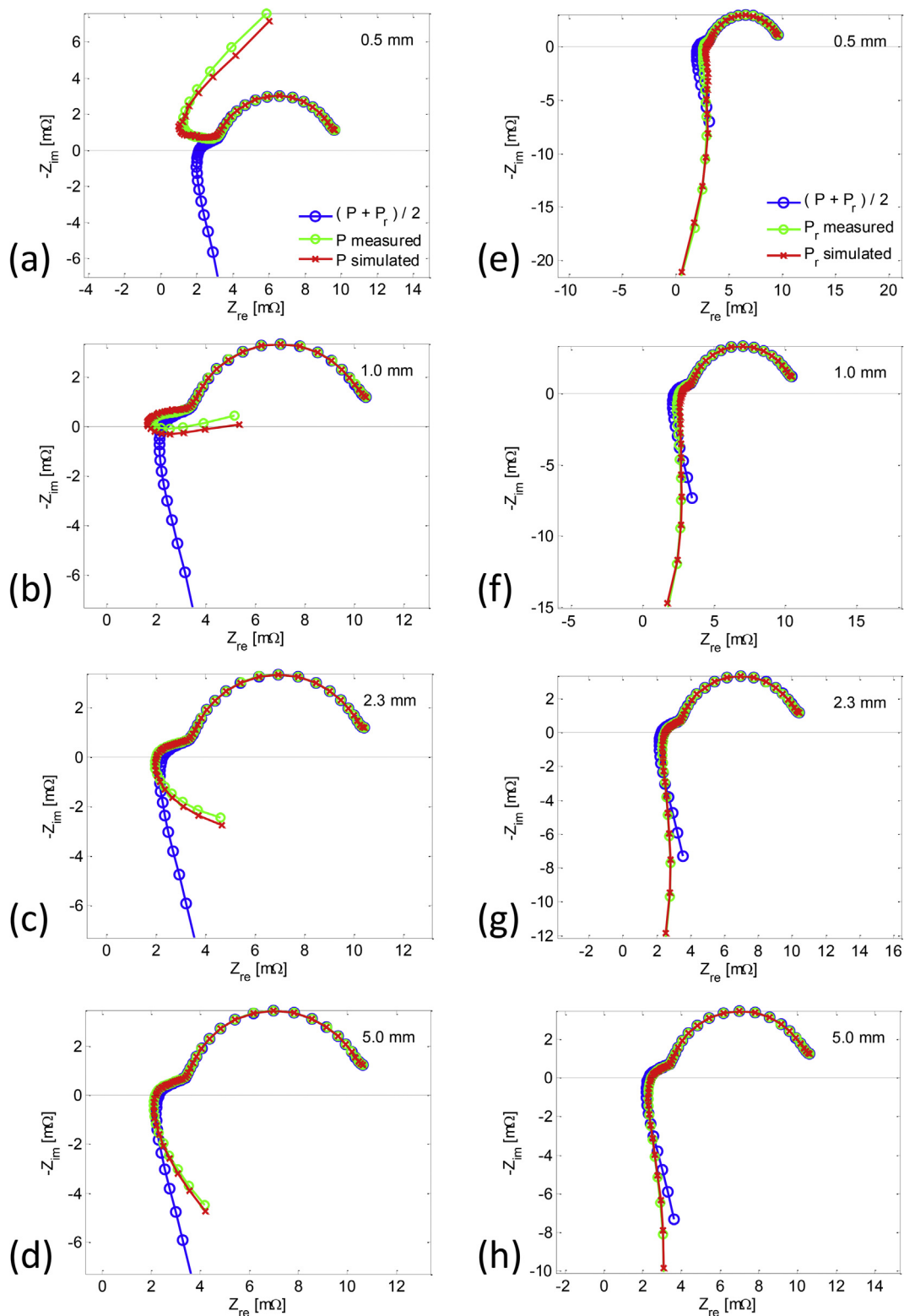
Fig. 9. Measured and simulated impedance spectra of P with respect to various μREF with indicated lengths (0.5, 1.0, 2.3 and 5.0 mm) obtained with standard (a–d) and reversed cable connection set-up (e–h). The blue curves show the compensated (averaged) impedance of P, the green curves show the measured (uncompensated) P impedance, including artefacts, and the red curves shows the uncompensated simulations.

Fig. 10. Measured and simulated impedance spectra on N with respect to various μREF with indicated lengths (0.5, 1.0, 2.3 and 5.0 mm) obtained with standard (a–d) and reversed cable connection set-up (e–h). The blue curves show the compensated (averaged) impedance of N, the green curves show the measured (uncompensated) N impedance, including artefacts, and the red curves shows the uncompensated simulations.

From these results it can be concluded that the individual impedance measurements of P, N, P_r and N_r in the high frequency range cannot be directly used since measurement artefacts are influencing these significantly.

The result of the new averaging method proposed in Section 3 is shown in Fig. 8. It can be seen that the impedance spectra of the P and N are now close to artefact-free in the high frequency range. The upward-bending behaviour of the summation impedance curve in Fig. 7a and the high frequency inductive tail found with the reversed measurement set-up in Fig. 7b are now completely disappeared, as shown by the red curve in Fig. 8. Moreover, the summation of the P and N impedance is in very good agreement with the Bat result (dark blue curve) along the whole frequency range. From these results it can be concluded that the proposed averaging method operates well and that the artefacts caused by the lead impedances can indeed be fully compensated. By applying this method the EIS measurements on three-electrode battery systems can be much more accurately analysed. In comparison to the capacitor bridge compensation method the proposed averaging method is also more accurate and easier to apply.

Similar artefacts were measured with another electrochemical measurement equipment (Ivium Technologies) and on smaller capacity three-electrode batteries in-house made with the Lithylene technology [10,40]. It was found that high frequency artefacts in all cases can be fully compensated by adopting this new compensation method. Moreover, measuring in the potentiostatic mode, *i.e.* applying an AC voltage and measuring the resulting AC current, resulted in similar artefacts as in the described galvanostatic mode but these can also be fully eliminated by the described compensation method.

4.4. Simulations

In order to validate the artefact models developed in Section 3, simulations are performed and compared with the impedance measurements. For the model simulations the true values for Z_P and Z_N should be known. However, these values are not known beforehand but can now be easily obtained from the compensated impedance measurements, described in Section 4.3. The models also require the input impedances for the measurement device (Z_{in}), the lead impedances (Z_l^i) and the various μREF impedances ($Z_{\mu REF}$). Since the μREF impedances have been determined experimentally (see Section 4.1) these values will be used as model input parameters in the simulations. Z_{in} and Z_l^i can then be determined by applying an optimization algorithm.

Figs. 9 and 10 compare the measured and simulated impedance results for the P and N electrode, respectively, measured with respect to the various μREF (0.5, 1.0, 2.3 and 5.0 mm). Since the artefacts are only minor for the longer μREF these results are therefore not shown. The blue curves show the compensated (averaged) measurements (Section 4.3). The green curves show the experimental results including measurement artefacts and the red lines show the simulations of the artefact models.

Fig. 9a–d shows the simulations for P (conventional configuration), using the model presented in Eq. (13). In Fig. 10a–d the same simulations are shown for the N (note that now Z_P is replaced by Z_N in Eq. (13)). From these results it can be concluded that the artefact model is in good agreement with the measurements for all μREF. Fig. 9e–h shows the simulations for P_r (reversed configuration) using the model presented in Eq. (22). Similarly, the same simulations are shown for N_r in Fig. 10e–h (note that Z_P is replaced by Z_N and *vice versa* in Eq. (22)). Again all simulation results are in very good agreement with the measurements.
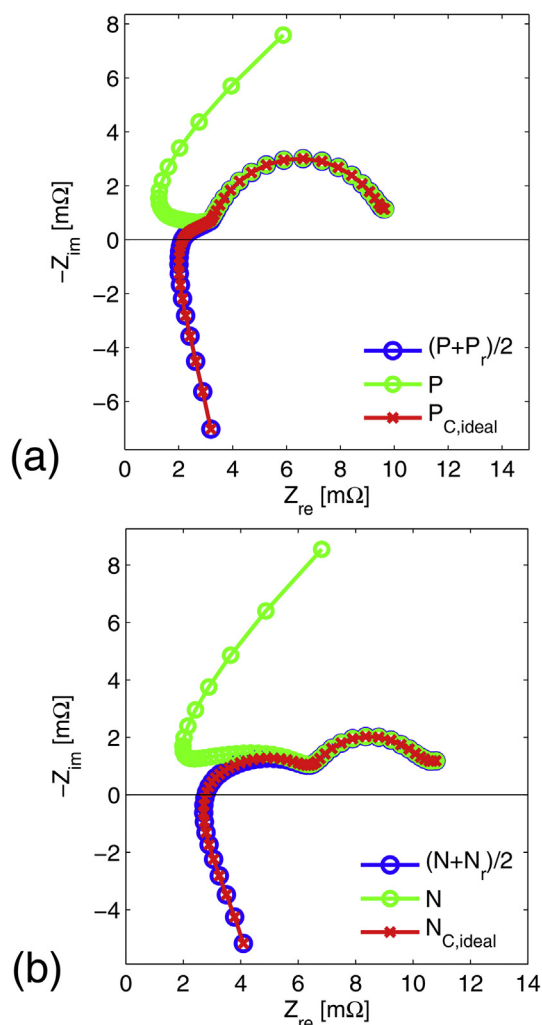

Fig. 11. Impedance spectra of P (a) and N (b) measured with respect to the μREF with the smallest tip length of 0.5 mm. Simulations with an ideal capacitor bridge (red) are compared to the proposed compensation method (blue). The measurements with artefacts are shown (green) for convenience.
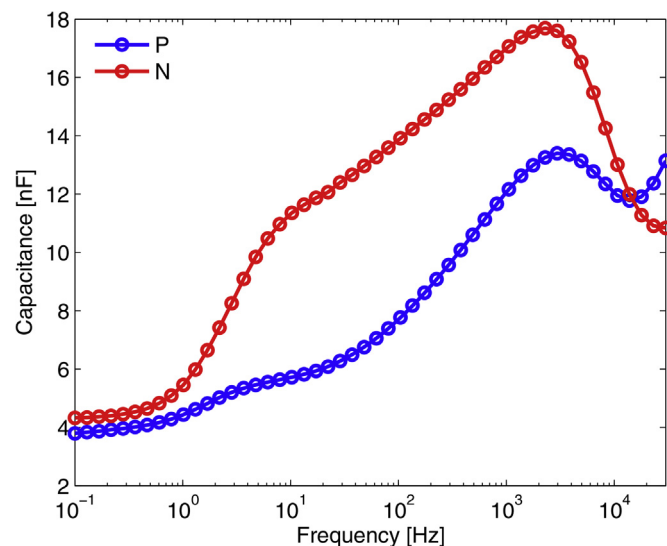

Fig. 12. Capacitance as a function of frequency for an ideal capacitor bridge.

In Fig. 11a and b the simulations with the ideal capacitor bridge (red line) are shown for P and N, respectively, simulated with respect to the 0.5 mm long µREF. For this simulation the model developed in Appendix A.3 is used in combination with the ideal capacitor bridge described by Eq. (17). It can be seen that the simulations are in perfect agreement with the averaged measurements for both P (a) and N (b) electrodes. Note that the compensated impedances (blue lines) described in Section 4.3 are shown for comparison.

Although the capacitor bridge simulations are in perfect agreement with the averaged measurements, it does not imply that the capacitance has a fixed value along the investigated frequency range. Using Eq. (18) the capacitance has been calculated for each frequency and the results are shown in Fig. 12 for both P and the N. These results clearly show that the capacitance, in the case of ideal compensation, indeed strongly depends on the frequency. This might explain why the capacitor bridge measurement results (Fig. 6), using fixed capacitor values, do not fully converge to the correct impedances. Comparing the simulated capacitances in Fig. 12 to the capacitances used in Fig. 6 it can be concluded that these are of the same order of magnitude. However, the values found in Fig. 12 are somewhat lower. This might be explained by the fact that the used equivalent circuit models are oversimplified with respect to the real measurement system where stray-capacitances, inductances and other circuitries inside the measurement device might be present. However, from the presented simulation results it can be concluded that the developed models qualitatively show good agreement with the measurements.

5. Conclusions

High-frequency three-electrode EIS measurement artefacts are found at Li-ion batteries with integrated lithium µREF. This makes a detailed impedance analysis of the individual electrodes unreliable and inaccurate. It has been found that EIS artefacts are a function of the µREF impedance, more particularly dependent on the active area of the µREF tip. The impedance of µREF electrodes should therefore be selected as small as possible in order to reduce these artefacts. However, large surface area µREF are not always favourable. Therefore, a method to compensate artefacts for high-impedance µREF has been developed, simply by averaging two individual three-electrode measurements. By using this method the measurement lead impedance, contributing significantly to artefacts, can be fully compensated. The proposed averaging method shows better results than measurements performed with an artefact-compensating capacitor bridge and is easier to apply. The proposed compensation method is therefore readily applicable to three-electrode electrochemical systems with high-impedance µREF.

Mathematical artefact models based on simplified equivalent circuit models have been developed. These models have been used to simulate the impedance measurements, including artefacts. The model simulations are in good agreement with the measurements.

Acknowledgements

Nomenclature

Symbol	Description	Unit
(H)EV	(Hybrid) Electric Vehicle	—
BMS	Battery Management System	—
EIS	Electrochemical Impedance Spectroscopy	—
CCCV	Constant current, constant voltage	—
Li(NMC)O$_2$	Lithium Nickel Manganese Cobalt Oxide	—
LiPF$_6$	Lithium hexafluorophosphate	—
REF	Reference electrode	—
µREF	Microreference electrode	—
Bat	Battery	—
P	Positive electrode	—
P$_r$	Positive electrode measured with reversed connections	—
N	Negative electrode	—
N$_r$	Negative electrode measured with reversed connections	—
WE	Working electrode connection measurement device	—
CE	Counter electrode connection measurement device	—
RE	Reference electrode connection measurement device	—
S	Sense connection measurement device	—
C	Capacitance capacitor bridge	F
ω	Angular frequency	rad/sec
I_{Bat}	Battery current, flowing between CE and WE connections	A
I_C	Current flowing through capacitor bridge	A
ΔV	Voltage difference between RE and S	V
K_1, K_2	Dimensionless modelling parameters	—
Z_{Bat}	True battery impedance	Ω
Z_{Bat}^m	Measured battery impedance	Ω
Z_P	True positive electrode impedance	Ω
Z_P^m	Measured positive electrode impedance	Ω
$Z_{P,r}^m$	Measured positive electrode impedance with reversed connections	Ω
$Z_{P,C}^m$	Measured positive electrode impedance in presence of capacitor	Ω
$\overline{Z_P^m}$	Averaged measured positive electrode impedance	Ω
Z_N	True negative electrode impedance	Ω
Z_N^m	Measured negative electrode impedance	Ω
$Z_{N,r}^m$	Measured negative electrode impedance with reversed connections	Ω
$Z_{N,C}^m$	Measured negative electrode impedance in presence of capacitor	Ω
$\overline{Z_N^m}$	Averaged measured negative electrode impedance	Ω
$Z_{µREF}$	Microreference electrode impedance	Ω
Z_{in}	Input-impedance measurement device	Ω
Z_C	Impedance of the capacitor bridge	Ω
Z_i^i	Lead and connection impedance of the measurement setup, where i can be WE, CE, RE, or S	Ω

Appendix A

By applying Kirchhoff's laws to the equivalent circuits in Fig. 2 and Fig. A1 the current flowing through the branches can easily be calculated. In Fig. A1 the equivalent circuits shown in Fig. 2 are reproduced. However, Fig. A1 also shows the current paths which are used to calculate the various currents flowing through the various circuits. Counterclockwise flowing currents are defined as positive and clockwise currents as negative. When these currents are known the voltage ΔV and the impedances can be calculated successively.

A.1. Battery impedance

In order to calculate the total measured battery impedance (Z_{Bat}^m) two linear equations need to be determined from the circuit shown in Fig. A1a. Following the current paths i_1 and i_2 we can write

$$(i_1 - I_{Bat})Z_l^{WE} + (i_1 - i_2)\left(Z_l^S + Z_{in}\right) = 0 \tag{A.1}$$

and

$$(i_2 - i_1)\left(Z_{in} + Z_l^S\right) + (i_2 - I_{Bat})(Z_P + Z_N) + i_2\left(Z_l^{RE} + Z_{in}\right) = 0, \tag{A.2}$$

respectively. This system of linear equations can be written in matrix notation to obtain a solution for i_1 and i_2, resulting in

$$MI = I_{Bat}Z \tag{A.3}$$

where

$$M = \begin{bmatrix} Z_{11} & -Z_{12} \\ -Z_{21} & Z_{22} \end{bmatrix}, \quad I = \begin{bmatrix} i_1 \\ i_2 \end{bmatrix}, \quad Z = \begin{bmatrix} Z_l^{WE} \\ Z_P + Z_N \end{bmatrix}. \tag{A.4}$$

Note that I is a vector with currents, not an identity matrix. In matrix M

$$Z_{11} = Z_l^{WE} + Z_l^S + Z_{in} \tag{A.5}$$

$$Z_{12} = Z_{21} = Z_l^S + Z_{in} \tag{A.6}$$

$$Z_{22} = 2Z_{in} + Z_l^S + Z_P + Z_N + Z_l^{RE}. \tag{A.7}$$

Solving A.3 by

$$I = M^{-1}I_{Bat}Z \tag{A.8}$$

for any arbitrary non-zero I_{Bat}, a solution can be obtained for both i_1 and i_2. Subsequently, the voltage difference ΔV can be calculated, according to

$$\Delta V = V_+ - V_-, \tag{A.9}$$

where

$$V_+ = i_2 Z_{in}, \quad V_- = (i_1 - i_2)Z_{in} \tag{A.10}$$

and therefore

$$\Delta V = Z_{in}(2i_2 - i_1). \tag{A.11}$$

The total measured battery impedance can finally be calculated by

$$Z_{Bat}^m = \frac{\Delta V}{I_{Bat}} = Z_{in}\frac{2i_2 - i_1}{I_{Bat}}, \tag{A.12}$$

in which I_{Bat} has the same value as in Eq. (A.8). From Eq. (A.12) it can be seen that Z_{Bat}^m is dependent on the input impedance of the measurement device multiplied with a current ratio. Obviously, i_1 and i_2 are dependent on the remaining impedances in the circuit.

A.2. Positive and negative electrode impedances

Following the circuit with current paths in Fig. A1b, the

measured impedances for the P (Z_P^m) can be derived. The current path i_1 is the same as in Eq. (A.1). However, the equation for current path i_2 becomes

$$(i_2 - i_1)\left(Z_{in} + Z_l^S\right) + (i_2 - I_{Bat})Z_P + i_2\left(Z_{\mu REF} + Z_l^{RE} + Z_{in}\right) = 0. \tag{A.13}$$

A system of two linear equations can be used in the same matrix notations and derivations as for the battery shown in Section A.1, *i.e.* Eq. (A.3) − (A.8). However, Eq. (A.7) changes into

$$Z_{22} = 2Z_{in} + Z_l^S + Z_P + Z_{\mu REF} + Z_l^{RE}, \tag{A.14}$$

and the second element in vector Z (see Eq. (A.4)) changes from $(Z_P + Z_N)$ to Z_P.

Solving the system of equations for i_1 and i_2 by Eq. (A.8) and using Eq. (A.9) − (A.12), Z_P^m can be calculated accordingly. The measured impedances for the N (Z_N^m), of which the equivalent circuit is shown in Fig. A1c, can be obtained with the same approach. Z_P has to be replaced by Z_N in the corresponding equations.

A.3. Capacitor bridge compensation

Fig. A1d shows the circuit in which a capacitor bridge is used to compensate the leakage current through the μREF. The capacitor creates one additional current path which must be considered, resulting in three paths in total. In order to calculate the measured P in the presence of a capacitor bridge ($Z_{P,C}^m$), a system of three linear equations must be solved. The equation for the current path i_1 is equal to Eq. (A.1). The equations for the current paths i_2 and i_3 become.

$$(i_2 - i_1)\left(Z_{in} + Z_l^S\right) + (i_2 - I_{Bat})Z_P + (i_2 - i_3)Z_{\mu REF} + i_2\left(Z_l^{RE} + Z_{in}\right) = 0 \tag{A.15}$$

and

$$i_3 Z_C + (i_3 - i_2)Z_{\mu REF} + (i_3 - I_{Bat})Z_N = 0, \tag{A.16}$$

respectively. In order to work towards a solution for the three currents Eq. (A.3) can be used, in which

$$M = \begin{bmatrix} Z_{11} & -Z_{12} & Z_{13} \\ -Z_{21} & Z_{22} & -Z_{23} \\ Z_{31} & -Z_{32} & Z_{33} \end{bmatrix}, \quad I = \begin{bmatrix} i_1 \\ i_2 \\ i_3 \end{bmatrix}, \quad Z = \begin{bmatrix} Z_l^{WE} \\ Z_P \\ Z_N \end{bmatrix}. \tag{A.17}$$

In Eq. (A.17) the elements Z_{11}, Z_{12}, Z_{21} and Z_{22} are equal to Eqs. (A.5), (A.6), (A.6) and (A.14), respectively. The remaining elements are defined as

$$Z_{13} = Z_{31} = 0 \tag{A.18}$$

$$Z_{23} = Z_{32} = Z_{\mu REF} \tag{A.19}$$

$$Z_{33} = Z_C + Z_{\mu REF} + Z_N. \tag{A.20}$$

By using Eq. (A.8) the currents i_1, i_2 and i_3 can be obtained. Eq. (A.9) − (A.12) can then be used to calculate $Z_{P,C}^m$. In order to calculate the measured impedance of the N ($Z_{N,C}^m$) all Z_P must be replaced by Z_N and *vice versa*.

A.4. Reversed electrode impedances

The circuit in Fig. A1e shows how P is measured with reversed connections ($Z_{P,r}^m$). Following the current paths i_1 and i_2 we can write

$$(i_1 - I_{Bat})\left(Z_l^{WE} + Z_N\right) + (i_1 - i_2)\left(Z_{\mu REF} + Z_l^S + Z_{in}\right) = 0 \quad (A.21)$$

and

$$(i_2 - i_1)\left(Z_{in} + Z_l^S + Z_{\mu REF}\right) + (i_2 - I_{Bat})Z_P + i_2\left(Z_l^{RE} + Z_{in}\right) = 0 \quad (A.22)$$

for both paths, respectively. Again, Eq. (A.3) can be used to solve this system of two linear equations in which the four elements of matrix M are defined as

$$Z_{11} = Z_l^{WE} + Z_N + Z_{\mu REF} + Z_l^S + Z_{in} \quad (A.23)$$

$$Z_{12} = Z_{21} = Z_{in} + Z_l^S + Z_{\mu REF} \quad (A.24)$$

$$Z_{22} = 2Z_{in} + Z_l^S + Z_{\mu REF} + Z_P + Z_l^{RE}. \quad (A.25)$$

Furthermore, vector Z in Eq. (A.3) is now defined as

$$Z = \begin{bmatrix} Z_l^{WE} + Z_N \\ Z_l^{RE} \end{bmatrix} \quad (A.26)$$

Solving the currents i_1 and i_2 by Eq. (A.8) and subsequently using Eq. (A.9) − (A.12), $Z_{P,r}^m$ can be obtained. The same approach can also be performed for determining $Z_{N,r}^m$, of which the schematic equivalent circuit is shown in Fig. A1f. However, in all corresponding equations Z_P must be replaced by Z_N and *vice versa*.
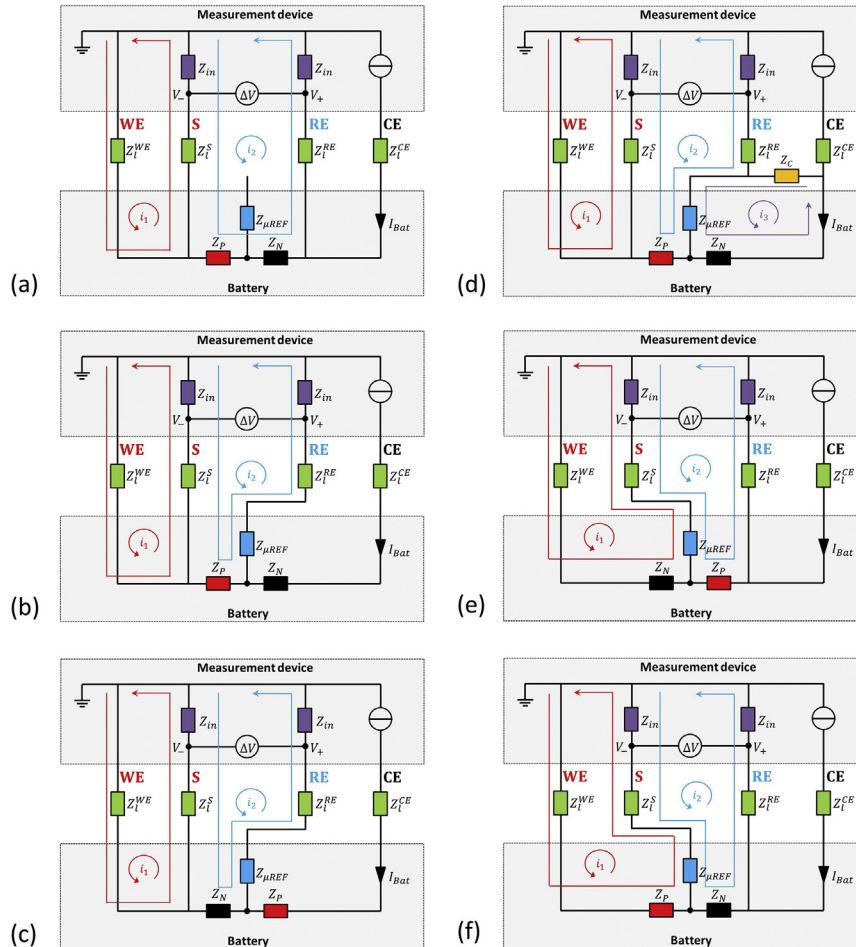
Fig. A1. Schematic equivalent circuits with indicated current paths for Bat (a), P (b), N (c), P with capacitor bridge (d), P with reversed connections (e) and N with reversed connections (f).

References

[1] M. Dolle, F. Orsini, A.S. Gozdz, J.-M. Tarascon, Development of reliable three-electrode impedance measurements in plastic Li-Ion batteries, J. Electrochem. Soc. 148 (2001) A851, https://doi.org/10.1149/1.1381071.

[2] M. Itagaki, K. Honda, Y. Hoshi, I. Shitanda, In-situ EIS to determine impedance spectra of lithium-ion rechargeable batteries during charge and discharge cycle, J. Electroanal. Chem. 737 (2015) 78–84, https://doi.org/10.1016/j.jelechem.2014.06.004.

[3] E. McTurk, C.R. Birkl, M.R. Roberts, D.A. Howey, P.G. Bruce, Minimally invasive insertion of reference electrodes into commercial lithium-ion pouch cells, ECS Electrochem. Lett. 4 (2015) A145–A147, https://doi.org/10.1149/2.0081512eel.

[4] G. Nagasubramanian, Two- and three-electrode impedance studies on 18650 Li-ion cells, J. Power Sources 87 (2000) 226–229, https://doi.org/10.1016/S0378-7753(99)00469-3.

[5] G. Nagasubramanian, D.H. Doughty, 18650 Li-ion cells with reference electrode and in situ characterization of electrodes, J. Power Sources 150 (2005) 182–186, https://doi.org/10.1016/j.jpowsour.2005.02.024.

[6] T. Osaka, D. Mukoyama, H. Nara, Review—development of diagnostic process for commercially available batteries, especially lithium ion battery, by electrochemical impedance spectroscopy, J. Electrochem. Soc. 162 (2015) A2529–A2537, https://doi.org/10.1149/2.0141514jes.

[7] J.Y. Song, H.H. Lee, Y.Y. Wang, C.C. Wan, Two- and Three-electrode Impedance Spectroscopy of Lithium-ion Batteries, vol. 111, 2002, pp. 255–267.

[8] M.-S. Wu, P.-C.J. Chiang, J.-C. Lin, Electrochemical investigations on advanced lithium-ion batteries by three-electrode measurements, J. Electrochem. Soc. 152 (2005) A47, https://doi.org/10.1149/1.1825385.

[9] Q. Wu, W. Lu, J. Prakash, Characterization of a commercial size cylindrical Li-ion cell with a reference electrode, J. Power Sources 88 (2000) 237–242, https://doi.org/10.1016/S0378-7753(00)00372-4.

[10] J. Zhou, P.H.L. Notten, Development of reliable lithium microreference electrodes for long-term in situ studies of lithium-based battery systems, J. Electrochem. Soc. 151 (2004) A2173, https://doi.org/10.1149/1.1813652.

[11] J. Zhou, P.H.L. Notten, Studies on the degradation of Li-ion batteries by the use of microreference electrodes, J. Power Sources 177 (2008) 553–560, https://doi.org/10.1016/j.jpowsour.2007.11.032.

[12] F. La Mantia, C.D. Wessells, H.D. Deshazer, Y. Cui, Reliable reference electrodes for lithium-ion batteries, Electrochem. Commun. 31 (2013) 141–144, https://doi.org/10.1016/j.elecom.2013.03.015.

[13] S. Solchenbach, D. Pritzl, E. Jia, Y. Kong, J. Landesfeind, H.A. Gasteiger, A Gold Micro-reference Electrode for Impedance and Potential Measurements in Lithium Ion Batteries, vol. 163, 2016, pp. 2265–2272, https://doi.org/10.1149/2.0581610jes.

[14] M. Klett, J.A. Gilbert, S.E. Trask, B.J. Polzin, A.N. Jansen, D.W. Dees, et al., Electrode behavior RE-visited: monitoring potential windows, capacity loss, and impedance changes in Li 1.03 (Ni0.5Co0.2Mn0.3)0.97O2/Silicon-Graphite full cells, J. Electrochem. Soc. 163 (2016) 875–887, https://doi.org/10.1149/2.0271606jes.

[15] A. Battistel, M. Fan, J. Stojadinović, F. La Mantia, Analysis and mitigation of the artefacts in electrochemical impedance spectroscopy due to three-electrode geometry, Electrochim. Acta 135 (2014) 133–138, https://doi.org/10.1016/j.electacta.2014.05.011.

[16] C. Bunzli, H. Kaiser, P. Novak, Important aspects for reliable electrochemical impedance spectroscopy measurements of Li-Ion battery electrodes, J. Electrochem. Soc. 162 (2014) A218–A222, https://doi.org/10.1149/2.1061501jes.

[17] D.W. Dees, A.N. Jansen, D.P. Abraham, Theoretical examination of reference electrodes for lithium-ion cells, J. Power Sources 174 (2007) 1001–1006, https://doi.org/10.1016/j.jpowsour.2007.06.128.

[18] C. Delacourt, P.L. Ridgway, V. Srinivasan, V. Battaglia, Measurements and simulations of electrochemical impedance spectroscopy of a three-electrode coin cell design for Li-Ion cell testing, J. Electrochem. Soc. 161 (2014) A1253–A1260, https://doi.org/10.1149/2.0311409jes.

[19] M. Ender, A. Weber, E. Ivers-Tiffée, Analysis of Three-Electrode Setups for AC-Impedance Measurements on Lithium-Ion Cells by FEM simulations, J. Electrochem. Soc. 159 (2012) A128, https://doi.org/10.1149/2.100202jes.

[20] Y. Hoshi, Y. Narita, K. Honda, T. Ohtaki, I. Shitanda, M. Itagaki, Optimization of reference electrode position in a three-electrode cell for impedance measurements in lithium-ion rechargeable battery by finite element method, J. Power Sources 288 (2015) 168–175, https://doi.org/10.1016/j.jpowsour.2015.04.065.

[21] S. Klink, D. Höche, F. La Mantia, W. Schuhmann, FEM modelling of a coaxial three-electrode test cell for electrochemical impedance spectroscopy in lithium ion batteries, J. Power Sources 240 (2013) 273–280, https://doi.org/10.1016/j.jpowsour.2013.03.186.

[22] S. Klink, E. Madej, E. Ventosa, A. Lindner, W. Schuhmann, F. La Mantia, The importance of cell geometry for electrochemical impedance spectroscopy in three-electrode lithium ion battery test cells, Electrochem. Commun 22 (2012) 120–123, https://doi.org/10.1016/j.elecom.2012.06.010.

[23] M.D. Levi, V. Dargel, Y. Shilina, D. Aurbach, I.C. Halalay, Impedance spectra of energy-storage electrodes obtained with commercial three-electrode cells: some sources of measurement artefacts, electrochim, Acta 149 (2014) 126–135, https://doi.org/10.1016/j.electacta.2014.10.083.

[24] H. Brandstätter, I. Hanzu, M. Wilkening, Electrochimica acta myth and reality about the origin of inductive loops in impedance spectra of lithium-ion electrodes — a critical experimental approach, Electrochim. Acta 207 (2016) 218–223, https://doi.org/10.1016/j.electacta.2016.03.126.

[25] M. Ender, J. Illig, E. Ivers-Tiffée, Three-electrode setups for lithium-ion batteries I. Fem-simulation of different reference electrode designs and their implications for half-cell impedance spectra, J. Electrochem. Soc. 164 (2017) 71–79, https://doi.org/10.1149/2.0231702jes.

[26] J. Costard, M. Ender, M. Weiss, E. Ivers-Tiffée, Three-electrode setups for lithium-ion batteries II. Experimental study of different reference electrode designs and their implications for half-cell impedance spectra, J. Electrochem. Soc. 164 (2017) 80–87, https://doi.org/10.1149/2.0241702jes.

[27] I. Jiménez Gordon, S. Grugeon, A. Débart, G. Pascaly, S. Laruelle, Electrode contributions to the impedance of a high-energy density Li-ion cell designed for EV applications, Solid State Ionics 237 (2013) 50–55, https://doi.org/10.1016/j.ssi.2013.02.016.

[28] D.D. Edwards, J. Hwang, S.J. Ford, T.O. Mason, Experimental limitations in impedance spectroscopy: Part V. Apparatus contributions and corrections, Solid State Ionics 99 (1997) 85–93.

[29] Y. Feng, G. Zhou, S. Cai, Explanation of high-frequency phase shift in ac impedance measurements for copper in low-conductivity media, Electrochim. Acta 36 (1991) 1093–1094.

[30] S. Fletcher, The two-terminal equivalent network of a three-terminal electrochemical cell, Electrochem. Commun 3 (2001) 692–696.

[31] G. Hsieh, S.J. Ford, T.O. Mason, L.R. Pederson, Experimental limitations in impedance spectroscopy: Part I - simulation of reference electrode artifacts in three-point measurements, Solid State Ionics 2738 (1996).

[32] F. Mansfeld, S. Lin, Y.C. Chen, H. Shih, Minimization of high-frequency phase shifts in impedance measurements, J. Electrochem. Soc. 135 (1988) 906–907.

[33] A. Tran, F. Huet, K. Ngo, P. Rousseau, Electrochimica Acta Artefacts in electrochemical impedance measurement in electrolytic solutions due to the reference electrode, Electrochim. Acta 56 (2011) 8034–8039, https://doi.org/10.1016/j.electacta.2010.12.088.

[34] C.C. Herrmann, G.G. Perrault, A.A. Pilla, Dual reference electrode for electrochemical pulse studies, Anal. Chem. 40 (1968) 1173–1174, https://doi.org/10.1021/ac60263a011.

[35] D.R. Baker, M.W. Verbrugge, X.X. Hou, A simple formula describing impedance artifacts due to the size and surface resistance of a reference-electrode wire in a thin-film cell, J. Electrochem. Soc. 164 (2017) A407–A417, https://doi.org/10.1149/2.1121702jes.

[36] L.H.J. Raijmakers, D.L. Danilov, J.P.M. Van Lammeren, M.J.G. Lammers, P.H.L. Notten, Sensorless battery temperature measurements based on electrochemical impedance spectroscopy, J. Power Sources 247 (2014) 539–544, https://doi.org/10.1016/j.jpowsour.2013.09.005.

[37] J.P. Schmidt, S. Arnold, A. Loges, D. Werner, T. Wetzel, E. Ivers-Tiffée, Measurement of the internal cell temperature via impedance: evaluation and application of a new method, J. Power Sources 243 (2013) 110–117, https://doi.org/10.1016/j.jpowsour.2013.06.013.

[38] H.P.G.J. Beelen, L.H.J. Raijmakers, M.C.F. Donkers, P.H.L. Notten, H.J. Bergveld, A comparison and accuracy analysis of impedance-based temperature estimation methods for Li-ion batteries, Appl. Energy 175 (2016) 128–140, https://doi.org/10.1016/j.apenergy.2016.04.103.

[39] L.H.J. Raijmakers, D.L. Danilov, J.P.M. Van Lammeren, M.J.G. Lammers, H.J. Bergveld, P.H.L. Notten, Non-zero intercept Frequency: an accurate method to determine the integral temperature of Li-Ion batteries, IEEE Trans. Ind. Electron 63 (2016) 3168–3178, https://doi.org/10.1109/TIE.2016.2516961.

[40] P.H.L. Notten, M. Ouwerkerk, H. van Hal, D. Beelen, W. Keur, J. Zhou, et al., High energy density strategies: from hydride-forming materials research to battery integration, J. Power Sources 129 (2004) 45–54, https://doi.org/10.1016/j.jpowsour.2003.11.019.